Journal Name

ARTICLE

Dipole Field Driven Morphology Evolution in Biomimetic Vaterite

Heather F. Greer[a], Ming-Han Liu[b], Chung-Yuan Mou[b] and Wuzong Zhou[a*]

Received 00th January 20xx,
Accepted 00th January 20xx

DOI: 10.1039/x0xx00000x

www.rsc.org/

Morphology evolution is an important process in naturally occurring biominerals. To investigate the interaction between biomolecules and inorganic components in the construction of biominerals, biomimetic hexagonal prism vaterite crystals were hydrothermally prepared through a reaction of urea with calcium nitrate tetrahydrate, whilst gelatin was added as a structure directing agent. An extraordinary morphology evolution was observed. The time dependent growth was investigated by using X-ray diffraction, scanning electron microscopy, transmission electron microscopy and thermogravimetric analysis. In the early stages, vaterite nanocrystallites, ~5 nm in diameter, underwent aggregation with gelatin molecules and precursor molecules into 50 nm sized clusters. Some nanoneedles, consisting of self-orientated nanocrystallites embedded within a soft gelatin matrix, were developed on the surface of disordered cores to form spherulite particles, with a similar morphology to natural spherulite biominerals. Further growth was affected by the high viscosity of gelatin, resulting in ellipsoid particles composed of spherulitically ordered needles. It is proposed that surface adsorbed gelatin induces the formation of dipoles in the nanocrystallites and interaction between the dipoles is the driving force of the alignment of the nanocrystallites. Further growth might create a relatively strong and mirror-symmetric dipolar field, followed by a morphology change from ellipsoidal with a cell-division like splitting, to twin-cauliflower, dumbbell, cylindrical and finally to hexagonal prism particles. In this morphology evolution, the alignment of the crystallites changes from 1D linear manner (single crystal like) to 3D radial pattern, and finally to mirror symmetric 1D linear manner. This newly proposed mechanism sheds light on the microstructural evolution in many biomimetic materials and biominerals.

Introduction

It is extraordinary that, in nature, the orientation of the building units of biominerals can self-adjust into various wonderful intricate morphologies, *e.g.* nacre,[1] abalone[2] and echinoderms[3] where many display single crystal-like properties. These fulfil many functions in nature, for instance, as structural support to provide protection to vertebrate skeletons and crustaceans.[4] In 1965, Hare and Abelson[5] discovered organic components accounted for 2 to 5 dry weight % of a nacreous shell. It was assumed the organic content present in this brick and mortar type arrangement of aragonite tiles would make their structure fragile. Surprisingly Jackson *et al.*[6] found that the work of fracture of these natural products was approximately 3000 times greater compared to that of pure $CaCO_3$ crystals. The high mechanical strength of nacre arose from the protein component binding to the outer surfaces of the aragonite building units. The adsorption of polymer is strong enough to tightly hold the plates together but weak enough to allow individual plates to shift from their original position to absorb the energy generated in the event of an extreme force being applied.[7]

Generally the formation mechanism, but especially the role of biomolecules in the construction of naturally occurring biominerals is not well established. To overcome this problem, inorganic crystals with similar morphologies are biomimetically synthesised in the presence of polymer or surfactants. It is believed that the ability of a structure directing agent to selectively adsorb onto a preferred surface allows the polymorphic phase, the nucleation, alignment of crystallites, and hence morphology to be stringently controlled.[8] Previous biomimetically prepared hierarchical morphologies include ZnO twin crystals,[9,10] ZnO twin cones[11] and calcite microtrumpets.[12] Simulating the structure of naturally occurring biominerals is also useful to understand the structure-function relationship. A great example is the first successful attempt of replicating nacre using $CaCO_3$ by Finnemore *et al*. Not only did the structure strongly resemble the biogenic material, its mechanical and optical properties could also be mimicked.[13]

For many decades $CaCO_3$ has been singled out as a vital ingredient in nature due to its high abundance in rock, the exoskeleton and tissues of marine organisms and in egg shells. The main application of $CaCO_3$ is in the construction industry but its high versatility allows its usage in other industrial applications including the manufacture of paints, plastics and pharmaceuticals.[14] Calcium carbonate precipitates as one of three anhydrous polymorphs, calcite, vaterite or aragonite. Phase diagrams have proven that calcite is the most thermodynamically stable and vaterite the least.[15] As the more

[a] EaStChem, School of Chemistry, University of St Andrews, Fife, KY16 9ST, United Kingdom. E-mail:wzhou@st-andrews.ac.uk
[b] Departments of Chemistry and Center of Condensed Matter Science, National Taiwan University, Taipei, Taiwan 10617.

† Electronic Supplementary Information (ESI) available: More SEM and TEM images, electron diffraction patterns, PXRD patterns, TGA plots. See DOI: 10.1039/x0xx00000x

soluble and least dense of the three polymorphs, vaterite is well known for transforming into a more stable polymorph upon contact with water.[16,17] Through dissolution and re-crystallisation, vaterite is said to convert to calcite at low temperature and aragonite at high temperature. A phase transformation in the opposite direction is also possible in some special conditions. For example, Mg substitution in calcite may greatly reduce its crystallinity and stability, leading to a transformation to aragonite, as we found in our previous study of hot spring travertines.[18] To obtain a preferred polymorph in laboratory, many factors such as pH, temperature and supersaturation have to be accurately controlled.[17,19]

Due to difficulties in obtaining large, pure, single crystals, the symmetry, space group, unit cell dimensions, orientation and site symmetry of the CO_3 ions in vaterite are controversial and have puzzled scientists for over half a century.[20,21] The first crystallographic structure of vaterite, a pseudo-hexagonal-orthorhombic structure with dimensions of a = 4.13, b = 7.15, c = 8.48 Å, space group Pbnm was proposed by Meyer in 1959, based on single crystal diffraction data.[22] All sites were reported as fully occupied which was not consistent with the apparent disorder. A second vaterite structural model, and now the most commonly accepted structure was proposed by Kamhi in 1963.[23] This structure with hexagonal symmetry and space group $P6_3/mmc$ has unit cell parameters of a = 4.13, c = 8.49 Å. This structure was proposed to have complete occupancy by calcium and 1/3 occupancy by the carbonate groups, which accounted for the considerable disorder. Kamhi reported that the weak reflections which could not be indexed were attributed to a superstructure, rotated 30° about the c-axis of Kamhi's original hexagonal structure, achieving unit cell parameters of $a = \sqrt{3}a' = 7.16$ Å and $c = 2c' = 16.98$ Å.[23] Recently, through the use of high-resolution synchrotron powder diffraction and aberration corrected HRTEM, at least two different crystallographic structures of vaterite were found to co-exist within a pseudo-single crystal.[24] The major phase had hexagonal symmetry whilst the minor phase, existing as nanodomains within the major matrix remains unknown. It has been suggested that this discovery may well explain the discrepancies between experimental and theoretical results and more importantly could have led to the proposal of low-symmetry structures for vaterite where an average of two structures may have been reported.[24,25] To avoid this, the structure of vaterite should be analysed on the scale of a few nanometres.

One of the most surprising and appealing biomimetic morphologies is spherulites, formed via intermediate sheaf and rod-like structures with a circular cross-section. This structure has been widely reported in a range of materials including $BaCO_3$, Bi_2S_3, $LnVO_4$ and $BiVO_4$[26-28] as well as naturally occurring zeolite stilbite.[29] Their formation typically follow a crystal splitting growth mechanism where nanoparticles forms a single rod which splits apart at both ends to form a sheaf or dumbbell-like structure. Previously, crystals have been found to evolve into a spherulite type structure as the growth process continued, either, with an increase in reaction time,[28] an increase in structure directing agent concentration[27] or a decrease in temperature.[30] Typically the splitting of crystals is associated with very rapid crystal growth but reports in literature have suggested that oversaturation of the solution and the inclusion of extra molecules into the crystal structure[29] were often factors to blame. Punin[31] stated that the crystal splitting is only possible if the oversaturation of a solution exceeds a "critical" value. Understandably, it is still an open question, and investigation of completely new factors and driving forces for the morphology control will be of great interest.

We report herein a new formation mechanism for polycrystalline hexagonal prism shaped vaterite prepared in the presence of gelatin as the structure directing agent. A novel multi-step morphology evolution process was observed, which is only possible when the structure consists of nanocrystallites embedded in a gelatin soft matrix. Initially a linear attachment of nanocrystallites resulted in spherulitically arranged needles. Polycrystalline ellipsoidal particles with high density of the needles underwent a cell-division like splitting, forming a twin-cauliflower like morphology. The central cylindrical component of the particles grew further by consuming the two cauliflower-like heads, resulting in a dumbbell-like shape. Finally, cylindrical shaped particles followed by hexagonal prism shaped particles appeared. The microstructural studies revealed that the patterns formed by the nanocrystallites matched the appearance of 'field force lines' first introduced by Michael Faraday in 1830s. The dipolar field induced morphology evolution proposed in the present work might be an important implication of what happens in many naturally occurring biominerals.

Results and discussion

Powder X-ray diffraction (PXRD) patterns of $CaCO_3$ specimens prepared with 28 g/L gelatin and 5.71 M urea but different reaction times are shown in **Fig. 1**. All samples are multiphasic. The sample after reaction of 3 h (**Fig. 1a**) contains four crystalline phases, two major and two minor. The dominant phases are Kamhi's hexagonal vaterite [23] (JCPDS card No. 24-0030) with the unit cell parameters of a = 4.13 and c = 8.49 Å, space group, $P6_3/mmc$ and rhombohedral calcite (JCPDS card No. 47-1743) with the cell parameters of a = 4.99, c = 17.06 Å, space group $R\bar{3}c$. The minor phases are orthorhombic aragonite (JCPDS card No. 41-1475) with the unit cell parameters of a = 4.96, b = 7.96, c = 5.74 Å, space group Pmcn and a precursor phase of monoclinic calcium nitrate urea (JCPDS card No. 44-0719) with the unit cell parameters of a = 9.248, b = 12.67, c = 7.688 Å, β = 113.54°, space group P21/c. Interestingly, the three polymorphs of $CaCO_3$ appear with distinguishable morphologies as shown in **Fig. S1, ESI†**, *i.e.* ellipsoidal hexagonal vaterite, rhombohedral or star-shaped rhombohedral calcite, and spindle-shaped orthorhombic aragonite. Their crystal structures were confirmed by high resolution transmission electron microscopic (HRTEM) images (**Fig. S1 d-f, ESI†**).

PXRD showed that, on increasing the reaction time from 3 h to 6 h, no calcium nitrate urea could be detected, confirming this is a precursor phase of $CaCO_3$. The morphologies of the rhombohedral and star-shaped rhombohedral calcite and spindle-shaped orthorhombic aragonite were unchanged in all the samples, according to the observations of scanning electron microscopy (SEM) and transmission electron microscopy (TEM). On the other hand, the morphology evolution of the vaterite particles with increasing reaction time is extraordinary (**Fig. 2**). Low magnification SEM images are displayed in **Fig. S2, ESI†**. In the present work, therefore, we focussed on the vaterite phase.

Low magnification SEM images of a specimen prepared after hydrothermal treatment for 6 h and using a low urea concentration

of 2.86 M (for slowing down the crystal growth) found that 3-4 µm sized particles consisting of needles arranged in a spherulitic manner (**Fig. 2a**) dominated the early stages of crystal growth. These particles further grew and increased their density to form ellipsoid shaped particles with an average particle size of 12 µm as shown by an example from a 3 h specimen prepared with a high urea concentration, *ca*. 5.71 M (**Fig. 2b**). It has been proved by SEM that these ellipsoid particles indeed consist of high density needles as discussed below.

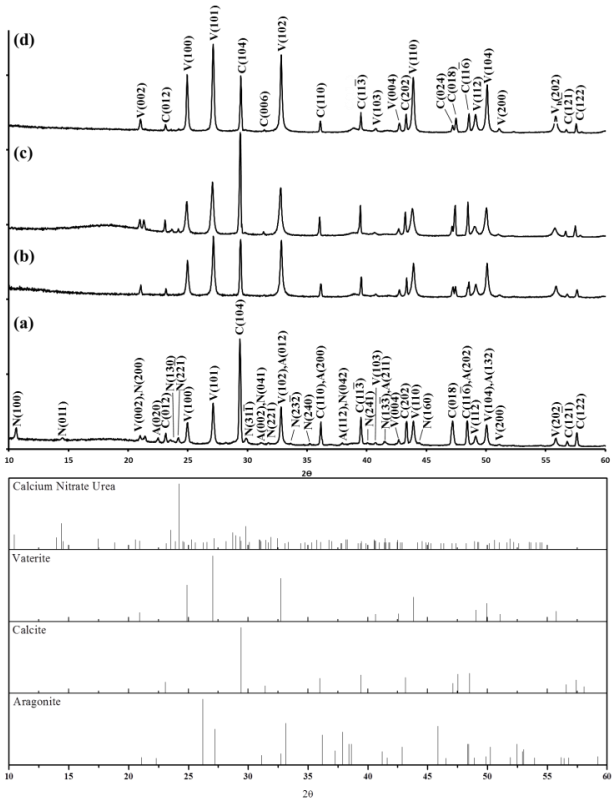

Fig. 1 PXRD patterns of specimens prepared using 28 g/L gelatin and 5.71 M urea with varying hydrothermal treatment times of, (a) 3 h, (b) 6 h, (c) 23 h, (d) 96 h. Pattern (a) is indexed to calcium nitrate urea (N), rhombohedral calcite (C), hexagonal vaterite (V) and orthorhombic aragonite (A) phases whilst pattern (d) is indexed to the rhombohedral calcite (C) and hexagonal vaterite (V) crystal structures, respectively.

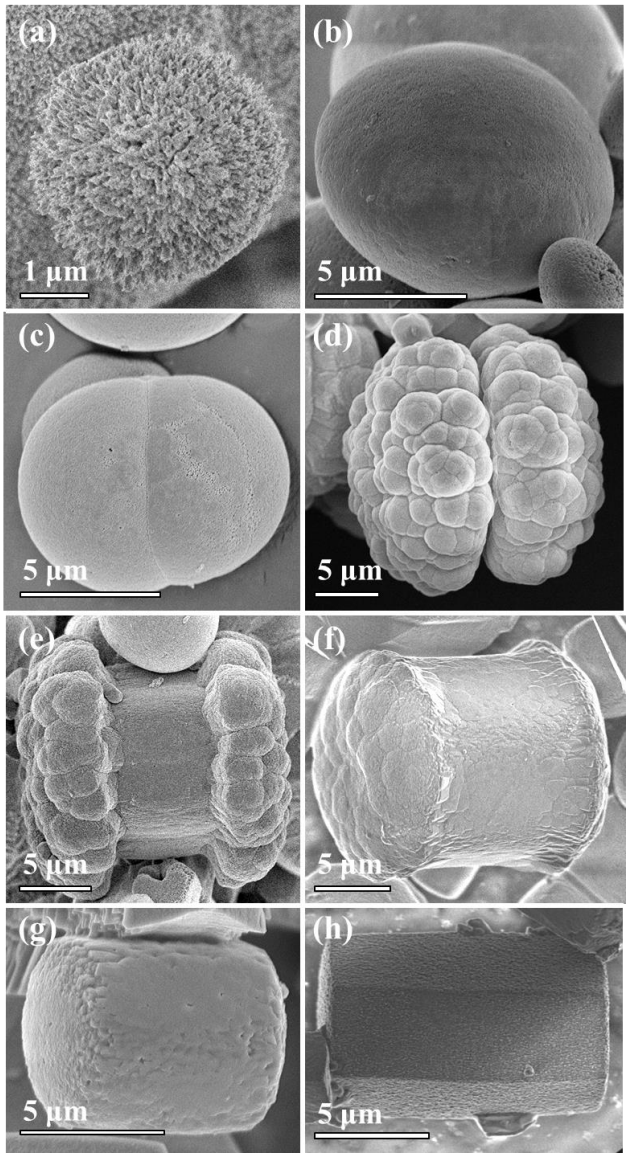

Fig. 2 SEM images of typical vaterite morphologies found after different lengths of hydrothermal treatment. (a) A ball of loose needles arranged in a spherulitic manner taken from the 6 h specimen specially prepared with a urea concentration of 2.86 M for slowing down the growth rate. Other images were from the samples prepared with 5.71 M urea and different hydrothermal treatment times: (b) and (c) 3 h, (d) 6 h, (e) 23 h, (f), (g) and (h) 96 h.

An equatorial notch rapidly developed on the surface of the ellipsoidal particles (**Fig. 2c**). On extending the heating time to 6 h, the main morphology changed to crystals with a twin-cauliflower like outer surface, while the particle dimension increased to ca. 22 µm, as shown by **Fig. 2d**. By 23 h a cylindrical 'waist' section had grown out from the central boundary to change the particle morphology from "twin-cauliflower" into "dumbbell" (**Fig. 2e**). During the next slower step, the dumbbell ends were partially consumed while the length of the cylindrical 'waist' greatly increased as shown in **Fig. 2f**. By 96 h, the dumbbell ends were completely consumed resulting in cylinder type particles (**Fig. 2g**). Finally, single crystal-like hexagonal prism particles formed (**Fig. 2h**), as a sign of the end of the morphology evolution.

Such a morphology evolution shown would be very unlikely if the particles are single crystals. If the particles are polycrystalline containing embedded nanocrystallites, the interaction between these nanocrystallites must play an important role in the morphology change. Another interesting phenomenon is that the vaterite phase dominates in the later samples. Control experiments of washing the final precipitate with ethanol instead of H_2O confirmed the calcite phase is not a result of a phase transformation of vaterite during the washing process. Since typically unstable vaterite did not undergo a phase transformation to calcite, it can be assumed that gelatin has a stabilising effect on vaterite. This effect was confirmed by synthesising 23 h specimens with lower gelatin concentrations, namely 7 g/L and 0 g/L. PXRD patterns shown in **Fig. S3, ESI†,** confirmed that the specimen prepared with 28 g/L gelatin very

slightly favoured calcite over vaterite, whereas when the gelatin concentration was significantly lowered to 7 g/L calcite very strongly dominated over vaterite. When no gelatin was added to the system calcite was the main polymorph with only a small quantity of vaterite and aragonite phases. A similar effect was observed by Guo *et al.* previously when different volume ratios of dimethylformamide and deionised water were applied.[32]

To confirm that gelatin forms composites with $CaCO_3$, thermogravimetric analysis (TGA) experiments were performed as shown in **Fig. S4, ESI†**. The 3 h, 23 h and 96 h specimens prepared with 28 g/L gelatin and a 23 h specimen prepared without gelatin all showed a dramatic weight loss of ~40 wt% corresponding to the decomposition of $CaCO_3$ into CaO and CO_2. Comparison between samples prepared with and without gelatin concluded approximately 6.1 to 9.5 wt% gelatin in the particles in the former depending on the length of hydrothermal treatment.

Higher magnification SEM, TEM, HRTEM images and SAED patterns were used to analyse the size, morphology and crystalline structure of the various growth stages in much greater detail. In this system $CaCO_3$ precipitated with a rapid growth rate as seen from the large well developed ellipsoid shaped crystals in **Fig. 2b**. To establish how this ellipsoidal morphology developed, synthesis conditions such as reaction time and urea concentration were reduced in order to slow down the reaction rate. No precipitate could be collected with reaction times of less than 2 h so experiments involving a reduction of the urea concentration were carried out. PXRD patterns of 6 h specimens prepared using 2.86 M and 5.71 M urea concentrations are shown in **Fig. S5**. Low urea concentrations were found to favour calcite over vaterite whilst higher urea concentrations favour the latter. By keeping the system slightly acidic through reducing the urea concentration to 2.86 M greatly retarded the growth of vaterite making it ideal conditions to study the very early stage crystallites, whereas higher urea concentrations (5.71 M) were more suitable to study the later stages of vaterite crystal growth.

The earliest morphology as detected by TEM imaging and SAED patterns was 5 nm sized spherical crystallites found in the 6 h (2.86 M urea) specimen (**Fig. 3a**). These nanocrystallites did not undergo further crystal growth, but aggregated randomly into larger (~50 nm in diameter) clusters with gelatin molecules as shown in **Fig. 3b**. The d-spacings of the marked crystalline fringes in **Fig. 3b** were measured as A: 3.35 Å and B: 3.46 Å, matching the (101) and (100) planes of vaterite. These d-spacings can also be indexed to the $(21\bar{2})$ and $(20\bar{2})$ planes of monoclinic calcium nitrate urea although it is expected that this phase would be unstable under the electron beam so vaterite is the more likely phase. The 50 nm sized clusters further aggregated into even larger particles, 300 to 400 nm in diameter (**Fig. 3c**).

Such an aggregation process was commonly observed as the first step in the so-called reversed crystal growth route.[33,34] However, surface re-crystallisation of the aggregates into a complete monocrystalline polyhedral shell did not take place in the vaterite particles in the present work. Instead, the clusters of nanoparticles underwent self-orientated attachment of small particles into loosely packed needles ordered in a spherulite manner as shown in **Fig. 3d**. Spherulitic growth has often been associated with a high viscosity or the presence of impurities.[35] In our case the high concentration (28 g/L) of gelatin in the system would have played a major role in the formation of these balls of needles, and this microstructure was not observed when the synthesis involved no gelatin. One possible reason is a dipole-dipole interaction, as Zhang *et al.*[36] demonstrated the dipole-induced self-assembly of nanocubes into one-dimensional chains.

In addition to the loose packing of the needles, each needle consists of many vaterite nanocrystallites embedded in disordered precursor/gelatin molecules as shown by the lower inset of **Fig. 3e**. One would have expected that these nanocrystallites are either randomly oriented or self-orientated along the longitudinal axes of individual needles. However, the most extraordinary structural feature is that SAED patterns attained from a large number of needles in a spherulite particle show a single crystal-like property as shown in the inset of **Fig. 3d**, indicating all the nanocrystallites in the particle, even from different needles are perfectly orientated although they are not directly connected to each other. D-spacings corresponding to the marked spots in the SAED pattern in **Fig. 3d** were measured as A: 3.49 Å and B: 3.54 Å and could be indexed to the (100) and (010) planes of vaterite. Further SAED evidence of this unusual single crystal-like spherulite phenomenon is shown in **Fig. S6, ESI†**. The SAED patterns taken from different locations within the same spherulite particle are almost identical with the same orientation.

The HRTEM image in **Fig. 3e** with a view direction of [001] confirms that needles in the spherulite particles consist of domains of small nanocrystallites with all the domains perfectly orientated. D-spacings measured from the marked spots are A: 3.54 Å and B: 3.52 Å, and can be indexed to the (100) and (010) planes of vaterite. The corresponding fast Fourier transform (FFT) pattern displayed in the upper inset confirms the well-ordered single crystal-like arrangement of nanocrystallites. Such a mosaic structure with all nanocrystallites embedded in a soft gelatin matrix is similar to the biomimetic fluorapatite–gelatine nanocomposites synthesized by Tlatlik, *et al.*, in which the crystallographic *c*-axis of the apatite nanocrystals are oriented parallel to the longitudinal direction of the fibrils.[37] When a ball of needles particle was crushed, loosely packed needles were seen to be radiating from a central disordered core of *ca*. 2 μm in diameter (**Fig. 3f**).

Although surfactant enhanced self-orientation of nanocrystallites is possible as observed previously,[38] such a process becomes very difficult in the balls of needles in this work since the connection between the nanocrystallites in neighbouring needles is poor. The nanocrystallites can even be disconnected inside a single needle. For the same reason, classical Ostwald ripening process cannot easily take place between loosely arranged needles. In other words, the interaction between the nanocrystallites, forcing them to rotate in a soft matrix of precursor/gelatin molecules to achieve self-orientation, must be three dimensional and can work in between nanoparticles with an unusual separation.

Hexagonal vaterite has a dipole moment along the *c*-axis, *i.e.* the (001) surface is terminated with positively charged Ca^{2+} cations whilst the $(00\bar{1})$ surface is terminated with negatively charged CO_3^{2-} anions. On the other hand, the isoelectric point of gelatin type B is in a range of 4.7 to 5.2.[39] At the early stages of crystal growth, *e.g.* 3 h with 28 g/L gelatin, 5.71M urea, the pH value of the synthesis system was detected to be 5.8 and the corresponding charge of gelatin molecules was slightly negative. The gelatin molecules can stabilize the (001) surface of the nanocrystallites where Ca^{2+} is the terminal

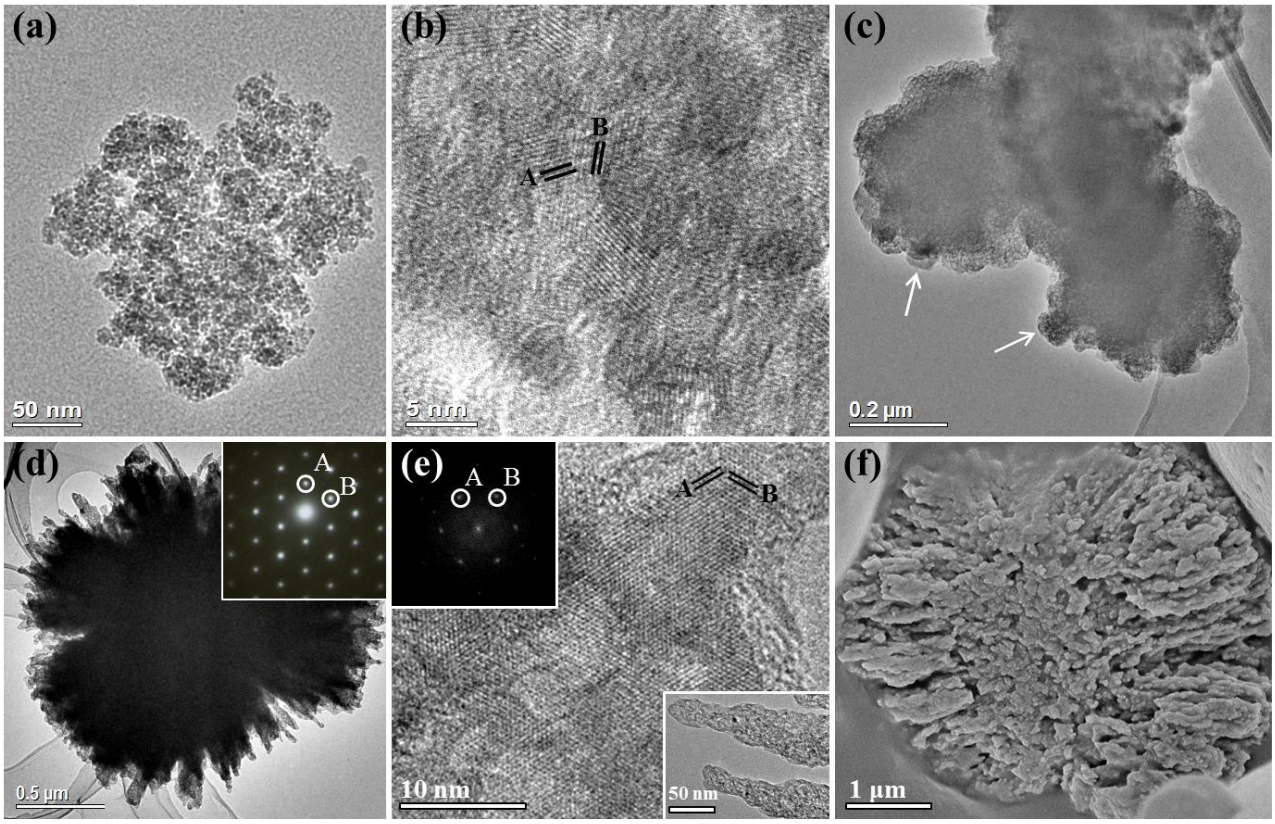

Fig. 3 SEM/TEM images of the vaterite phase from the 6 h specimen (28 g/L gelatin, 2.86 M urea). (a) TEM image of an aggregate of 5 nm sized crystallites. (b) HRTEM image of a selected area in (a) showing vaterite nanocrystallites embedded in disordered precursor/gelatin molecules. The crystal fringes marked A and B can be indexed to the (101) and (100) planes of vaterite, respectively. (c) TEM image of clusters of weakly crystalline nanoparticles (50 nm in diameter) as indicated by the arrows. (d) TEM image of a ball of needles particle produced by self-orientated attachment of nanoparticles. The inset is a corresponding SAED pattern recorded from a large area covering many needles. (e) HRTEM image taken at the edge of a spherulite particle showing a single crystalline-like domain structure with marked fringes indexed to A (100) and B (010) planes of vaterite. The upper inset is the corresponding FFT pattern. The lower inset is a low magnification TEM image of individual needles found at the edge of a spherulite particle. (f) SEM image of a broken ball of needles, showing the core area contains no needle morphology.

layer, and enhance the formation of a dipolar field in each nanocrystallite. In a bulk crystal, such a dipolar field is extremely weak. However, in a nanocrystallite, the relative strength of the dipolar field could be significant. These nanocrystallites embedded in a soft precursor/gelatin matrix have some degree of freedom to rotate and shift locally. These vaterite nanocrystallites can be regarded as nano-dipoles. The interactions between these dipoles resulted in a linear arrangement of nanocrystallites to form nanoneedles. However, such an alignment was not observed, probably because all the nanocrystallites in the spherulite particles soon re-aligned into a uniform orientation.

The balls of needles underwent further aggregation to form larger ellipsoid shaped crystals with a relatively smooth surface and an average particle size of 12 µm (**Fig. 2b**). The ellipsoid particles consist of a significantly denser spherulitic arrangement of needles compared to the previous stage as demonstrated by a SEM image of a broken ellipsoid crystal (**Fig. 4a**). A higher magnification SEM image in **Fig. 4b** found the 1 µm core region to be notably empty, due to losing the disordered and potentially amorphous $CaCO_3$ core.

High resolution SEM imaging of the surface of an ellipsoid crystal found the tips of needles with a diameter of 40 nm protrude from the surface (**Fig. 4c**). Like the balls of loose needles, the ellipsoid particles retain the single crystalline-like arrangement of nanocrystallites as proven by HRTEM and SAED (**Fig. S7, ESI†**). A HRTEM image and corresponding FFT pattern of needles in an ellipsoid particle is shown in **Fig. 4d**. The domain structure of an individual needle can be seen with perfectly orientated crystal fringes measuring A: 3.47 Å and B: 8.58 Å which can be indexed to the (010) and (001) planes of vaterite. The lightly contrasted areas show the high porosity of the microsized ellipsoids caused by two main aspects, the inclusion of gelatin molecules and the voids typically produced with spherulitic growth. In addition, HRTEM images and SAED patterns (**Fig. S7, ESI†**) established the longest dimension of the ellipsoid particles is along the [001] zone axis.

Rapidly after the formation of ellipsoid shaped particles, an equatorial notch developed on their surface as shown in **Fig. 2c**. Yao *et al.*[40] prepared similar twinned spherical vaterite crystals under the control of poly(L-lysine) and suggested they formed from the aggregation of nanoparticles into a nuclear plate followed by the assembly of nanoparticles onto both sides of the plate. Our observation, however, indicates that the starting point of this equatorial notch must be at the centre of the ellipsoid particles, where re-crystallisation of the disordered core into hexagonal vaterite took place. As associated with this change the crystallinity and particle size in the core region would increase. Due to the highly compact arrangement of needles in the ellipsoidal particles it can be

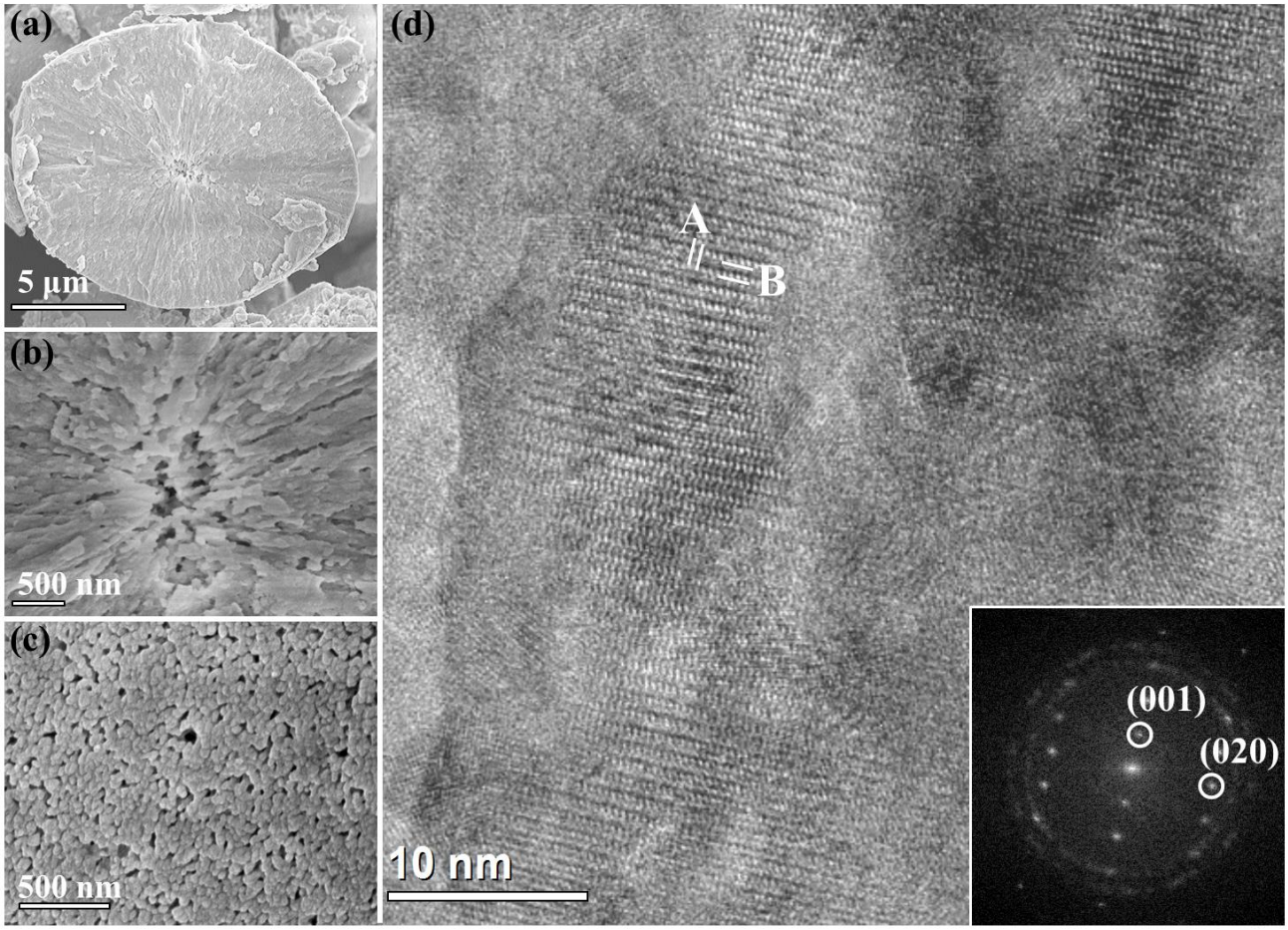

Fig. 4 SEM/TEM images of the vaterite phase from the 3 h specimen (28 g/L gelatin, 5.71 M urea). (a) Low magnification SEM image of a broken ellipsoid particle similar to that in **Fig. 2b** where the inner structure consists of densely packed needles. (b) An enlarged SEM image of the 1 µm sized core region of the particle in (a) showing the core to be empty. (c) High magnification SEM image of the surface of an ellipsoid particle where needles, *ca.* ~40 nm in diameter were found to radiate from the centre to the surface. (d) HRTEM image of a needle in an ellipsoidal particle (FFT pattern is shown inset) showing a domain structure with perfectly orientated fringes indexed to vaterite.

deduced that only a small build up in pressure associated with the growth of the central disc would be required to instigate splitting.

On extending the heating time to 6 h (5.71 M urea, 28 g/L gelatin), the embryonic-type particles changed their morphology into those with a very rough outer surface as shown in **Fig. 2d** accompanied by a significant increase in particle size (20-25 µm). Fortunately, in our system the two parts of the cauliflower-like twinned structures were only weakly attached to each other through the central boundary hence they were easily broken as shown in **Fig. 5a**. When the twin cauliflower structures were broken their structure resembled a flower where large 'petals' projected from a disc in the core. The petals do not appear to be disturbed indicating only the small core section is involved in the bonding between alike crystals. Twin cauliflower particles containing a disc with a smaller dimension are most likely that at an earlier growth stage (**Fig. S8, ESI†**). To gain a greater insight into the structure and orientation of the disc a 200-300 nm thick slice of a twin cauliflower particle was prepared by focussed ion beam (FIB) (**Fig. 5b**). TEM investigations of the disc in the core (marked by a box in **Fig. 5b**) found it consists of two thin plates (marked by two short arrows in **Fig. 5c**) with a uniform diameter and thickness of 5 µm and 200 nm, respectively. A pale contrasted region exists between the plates.

This core particle is remarkably similar to ZnO/gelatin twinned platelets found by Bauermann *et al.,*[39] Greer *et al.*[10] and Liu *et al.*[41] where it was suggested that the 2-3 nm separation between the layers was a very thin layer of gelatin molecules. The key step in the formation mechanism was proposed to be surface re-crystallisation of $Zn_5(NO_3)_2(OH)_8{\cdot}2H_2O$/gelatin composite sheets into ZnO. A negatively charged gelatin layer, sandwiched between two ZnO crystalline sheets, induced negatively charged outer surfaces of this double-layer particle, which served as a core offering a pair of strong mirror symmetric central dipolar fields to guide the formation of twin particles.[10,41]

The disc in the centre of an ellipsoidal particle as shown in **Fig. 5a** may also be a base of central dipolar field. A similar $CaCO_3$ ellipsoidal morphology and particle splitting to **Fig. 2c** has also been observed by Imai *et al.* They believed the origin of the particle splitting was at its centre, although dipolar field interactions was not mentioned.[42]

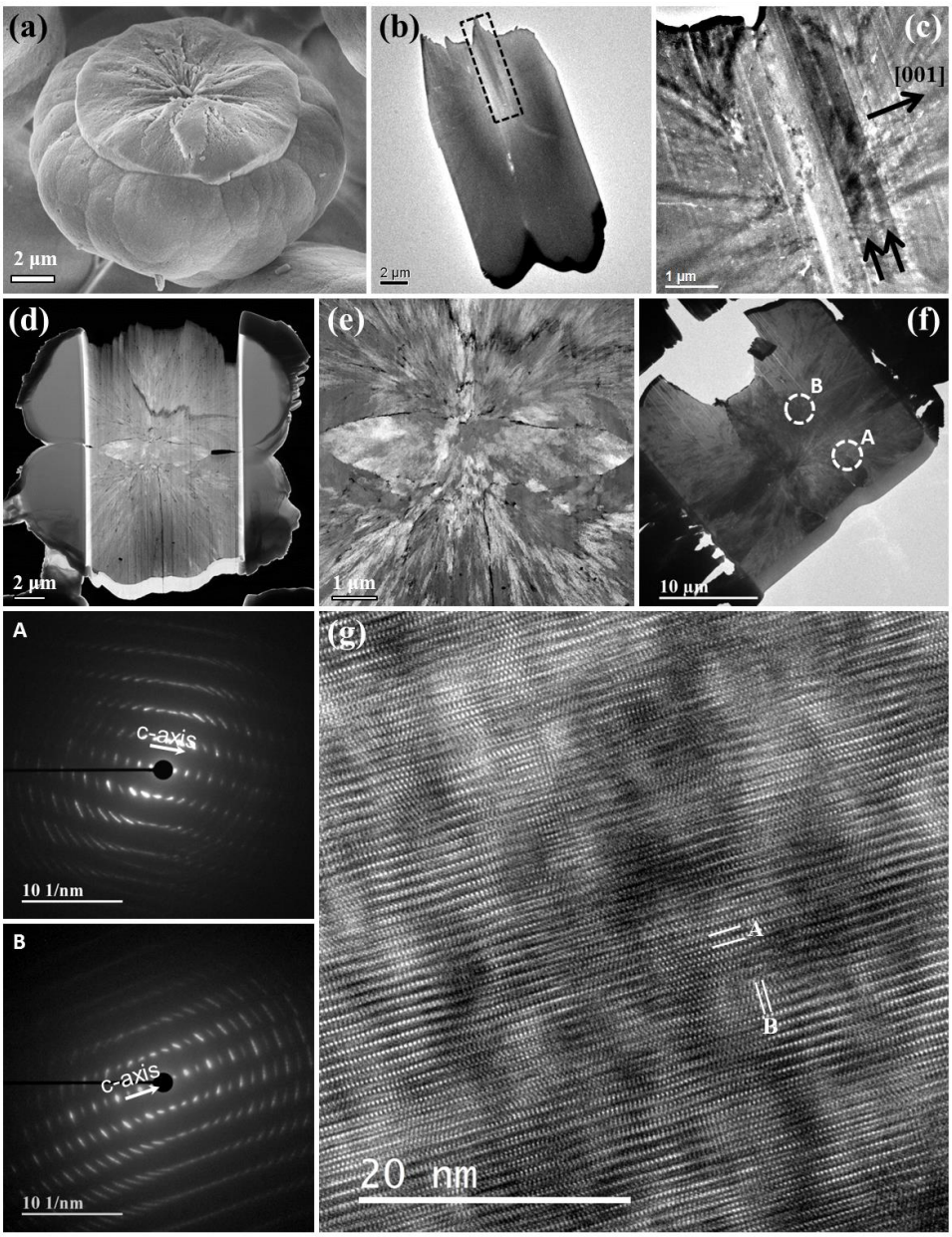

Fig. 5 Electron microscopic images and diffraction patterns recorded from twin-cauliflower particles. (a) SEM image of a twin cauliflower-like particle broken in half to reveal a large disc-like core section. (b) TEM image of a thin section of a twin cauliflower particle prepared by FIB. The core of the particle is marked by a box. (c) Higher magnification TEM image of the core region of the particle in (b) showing a double plate structure as marked by two arrows. (d) ADF STEM image recorded from a thin cross section of a twin-cauliflower particle prepared by FIB. (e) A higher magnification ADF STEM image of the core particle in (d). (f) TEM image of a thin section of a twin-cauliflower particle prepared by FIB. The SAED patterns, assigned A and B were recorded from the marked regions, respectively. Comparison of SAED patterns shows a 31° rotation in the c-axis. (g) HRTEM image recorded from a thin section of a twin-cauliflower particle demonstrating a single crystal-like domain structure. The crystalline fringes marked A and B can be indexed to the (001) and (100) planes of hexagonal vaterite.

On investigation of a second thin section of a twin-cauliflower particle by annular dark field scanning transmission electron microscopy (ADF STEM), the 3D radial arrangement of needles surrounding the core particle became apparent (**Fig. 5d**). A higher magnification ADF STEM image (**Fig. 5e**) of the core particle confirms that it is constructed from densely packed nanoparticles whilst many pores can be observed in the surrounding needles. SAED patterns marked A and B were recorded from two different locations on the same twin-cauliflower thin section (**Fig. 5f**), with the corresponding regions marked A and B, respectively. Although both SAED patterns show the same [010] view direction of hexagonal vaterite, it was noted that the *c*-axis had rotated by 31° indicating the nanocrystallites are radially aligned from the core. Since all nanocrystallites in the particles are not parallel to each other, the

diffraction spots are diffused, where the degree of diffusion is dependent on the size of the area covered by the electron beam. The ADF STEM image of a cross section of a twin-cauliflower particle in **Fig. 5e** shows a central disc and radial contrast patterns on both sides, which is similar to the famous Faraday's iron filing patterns in the 19th century, when he sprinkled iron filings on a sheet of paper beneath which there was a magnet. The latter revealed a theory on magnetic lines of force, while the former shows how vaterite nanocrystallites align along possible force lines of a dipolar field created from the central disc.

The HRTEM image of a twin-cauliflower 'petal' in **Fig. 5g** shows a domain structure of nanocrystallites with an average size of 7 nm where well orientated lattice fringes were measured as A: 8.49 Å and B: 3.52 Å and could be indexed to the (001) and (100) planes of vaterite. A few years ago Matsumoto *et al.*[43] prepared ZnO microspheres in the presence of polyethylene glycol with a microstructure consisting of wedge nanocrystallites radially aligned along the *c*-axis. This was thought to be the first time polycrystalline particles exposing only one specific crystal plane, in this case only the c(+)-plane, *i.e.* the positively terminated face of the (001) plane, was exhibited. It was suggested that particles with this type of structure should have unique properties such as enhanced photocatalytic abilities.

After hydrothermal treatment for 23 h the main morphology of the vaterite crystals had changed to a dumbbell type structure (**Fig. 2e**). Initially it was thought the cylindrical 'waist' of the dumbbells grew out from the central boundary of the twin cauliflower-like structures, but after careful measurements, it was found that the longitudinal dimension of the particles had in fact decreased from 20-25 µm to 18-22 µm, and the 'cauliflower' heads reduced as well. Therefore, the dumbbell structures must have developed from the reorganisation of the nanocrystallites within the needles into a more parallel, compact layout. In other words, the growth of the cylindrical 'waist' is based on the cost of 'cauliflower' heads. The SEM image in the inset of **Fig. 6a** shows the needles making up the head of the dumbbells remained unchanged during the morphology change from twin cauliflower-like to dumbbell shaped particles. The high magnification SEM image in **Fig. 6a** shows the needles has an irregular cross section with a dimension of 100-150 nm. The diameter of the needles increased significantly from 40 nm (**Fig. 4c**) in the ellipsoid particles. The high magnification SEM image of the 'waist' of a dumbbell particle in **Fig. 6b** shows it consists of needles aligned in a parallel manner. If several needles have the same orientation they could fuse together into thicker needles such as those marked by the arrows in **Fig. 6a**, and even larger blocks as indicated in **Fig. 6b**. Again, these are likely large areas with higher crystallinity which formed after the re-crystallisation of needles with the same orientation. The merging of several single crystal-like areas created a much smoother outer surface as shown in **Fig. 2f**. At this stage it was noticed that the majority of needles had reorganised into a parallel arrangement thus the length of the 'waist' section increased.

When all needles had re-orientated from radial into a parallel manner, the particles had a cylindrical morphology similar to that shown in **Fig. 2g**. TEM imaging of a cylindrical type particle (inset of **Fig. 6c**) found it is built from nanorods with a diameter of 5 nm and a length of 30–40 nm. In general, the nanorods appear to be well aligned in a parallel manner although some distortion in this particle would have arose from the fracturing of the crystal when intentionally crushed. HRTEM (**Fig. 6d**) established that the rods are partially orientated in some areas whilst other areas consisted of large single crystal-like domains. Generally large single crystal-like areas were located nearer the surface region of the cylindrical particles whereas partially orientated areas tended to be located towards the centre of the crystals. This finding is similar to that discovered by Chen *et al.*[34] in zeolite analcime where crystalline surface 'islands' could self-adjust their orientation before fusing together to form a thin single crystalline icositetrahedral shell comprising 24 identical {211} facets whilst the core remained polycrystalline.

The final hexagonal prism morphology (**Fig. 2h**) formed at a late stage (96 h) after surface re-crystallisation occurred on a larger scale. This step is thought to be similar to the two step mechanism initially found by Zhan *et al.*[44] in $CaCO_3$ and later in ZnO by Jitianu and Goia,[45] where polycrystalline cylinders were rapidly yielded from the aggregation of nanoparticles. This step was too fast to allow a more complex morphology to develop so was followed by a very slow second stage where the nanoparticles were able to rearrange into hexagonal prisms. Performing HRTEM on several nanorods located near the surface of a hexagonal prism particle found a perfectly orientated domain structure confirming all nanocrystallites within the rods had the same orientation plus all neighbouring nanorods were perfectly orientated with each other (**Fig. 6e**). The marked lattice fringes in **Fig. 6e** were measured as A: 2.72 Å and B: 3.54 Å with an interplane angle of 67°, and can be indexed to the (102) and (010) planes of vaterite. Although the nanorods are perfectly orientated with each other some defects exist in the boundary between neighbouring needles.

SAED was performed on hexagonal prism vaterite particles to determine their growth direction. The single crystal-like SAED pattern shown in the inset of **Fig. 6f** was recorded from the area marked by a square on a hexagonal vaterite particle with a smooth surface. However, the SAED pattern indicates co-existence of a superstructure and stacking faults. D-spacings calculated from the marked spots were measured as A: 4.07 Å and B: 2.01 Å, which could be indexed to the (002) and (110) planes of the basic hexagonal vaterite with a = 4.02 and c = 8.14 Å. In between spots A and B, there are two rows of weak spots. These spots can be indexed to a superstructure, $\sqrt{3} \times \sqrt{3} \times 2$ derived from the basic unit cell, which is similar to that reported by Kamhi in 1963.[23] Consequently, the spots A and B will be indexed to the superunit cell as (004) and (300). All the weak spots can be indexed accordingly. All diffraction spots along the [001] direction were diffuse indicating the presence of many defects along the *c*-axis. The corresponding HRTEM image shown in **Fig. S9, ESI†** demonstrates a large number of layered defects along the [001] direction. The SAED pattern combined with HRTEM images also established that the *c*-axis is parallel to the long axis of the hexagonal prism. Similar stacking faults along the [001] zone axis was observed in vaterite tablets of freshwater lacklustre pearls [46] and Herdmani momus spicules.[24] In the latter example HRTEM images and diffraction patterns showing that the stacking faults were found to be in good agreement with the Kamhi vaterite structure where diffuse scattering perpendicular to the c-axis is well known.[23] Qiao and Feng reported that these stacking faults may increase the stability of vaterite.[46]

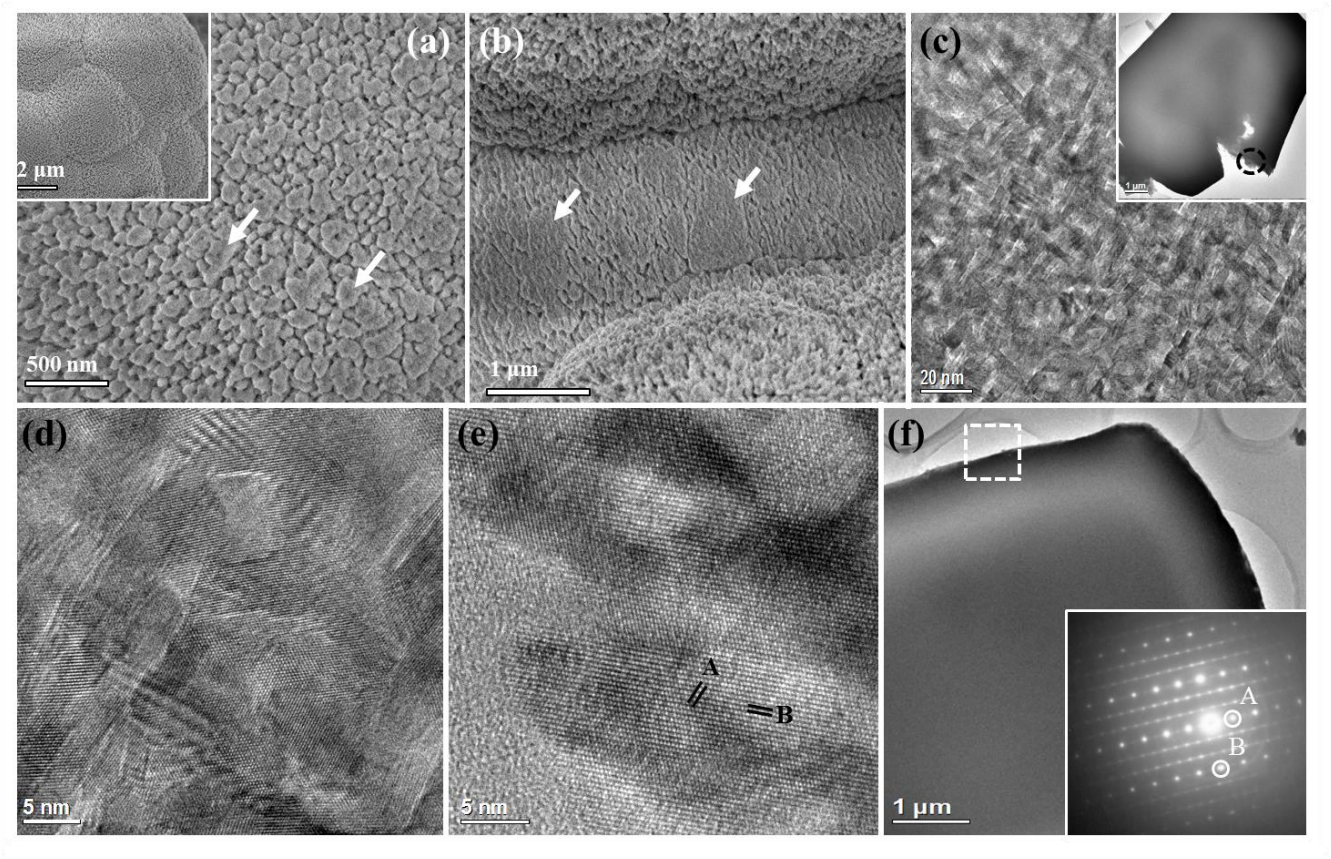

Fig. 6 Electron microscopic images recorded from a dumbbell, a cylindrical and a hexagonal prism particle. (a) HR-SEM image of the needles making up the head of the dumbbell-like structure revealing the needles have an irregular cross section with a diameter of approximately 100-150 nm. The arrows mark regions where several needles have re-crystallised together. A lower magnification SEM image is shown in the inset. (b) SEM image of the 'waist' section of a dumbbell showing well aligned needles. The arrows mark possible large single crystal areas. (c) TEM image of nanorods aligned in parallel recorded from the area marked by a circle in the fractured cylindrical particle shown in the inset. (d) HRTEM image of the rods in (c). The lattice fringes are partially orientated in some areas whilst other regions contain large single crystal-like domains. (e) HRTEM image of nanorods located at the edge of a hexagonal prism particle. The marked d-spacings measured from the single crystal-like fringes are A: 2.72 Å and B: 3.54 Å. (f) TEM image of a hexagonal prism particle. The inset is the corresponding single crystal-like SAED pattern recorded from the area located within the square. The marked d-spacings measured from the spots are A: 4.07 Å and B: 2.01 Å. Some weak diffraction spots indicate a $\sqrt{3}$ X $\sqrt{3}$ X 2 superstructure.

According to the microstructural studies, the reorganisation of needles into a parallel alignment began at the core of the twin cauliflower particles where the double nanoplate structure resides. The reorganisation of needles can be explained using a dipole field directed mechanism where polycrystalline structures are composed of nanocrystallites embedded in a gelatin matrix; therefore the nanocrystallites are able to rotate when directed by dipole field lines. Dipole field directed mechanisms have previously been reported by theoretical calculations in $BaTiO_3$[47] and experimentally in fluorapatite[48-50] and ZnO[10] systems where gelatin was added as the structure directing agent. In both cases the addition/reorganisation of needles/plates was along the [001] growth direction due to the dipole moment in fluorapatite and ZnO along the *c*-axis. Additionally, intrinsic dipole field controlled mechanisms have been proposed in all three anhydrous polymorphs of $CaCO_3$.[51-53]

Until now only the reverse rod-to-sphere formation mechanism has been reported, where Kniep and co-workers[48,49,54] imaged the location of intrinsic electric dipole fields using electron holography and used the MAFIA program to determine their intensities. Their proposed model demonstrated how dipole field force lines could have directed the growth around the polar hexagonal fluoroapatite/gelatin rods to form a dumbbell then an embryonic type morphology and finally to a spherulite-type crystal. Their model was used to explain the alignment and branching of single crystalline fibrils from a hexagonal seed through the bending of fibrils rather than rotation of nanocrystallites within the needles which occurs in our reverse spherulite to hexagonal prism route. Although Kniep and co-workers[55] claimed the dipolar property of their fluoroapatite-gelatin system stems from the triple helix in gelatin lining up in parallel, analysis of our vaterite-gelatin structures suggests the dipolar property likely stems from the dipole moment of the inorganic vaterite component and not the gelatin molecules.

Formation mechanism

Based on our extensive analysis of specimens at various growth stages we are now able to propose a mechanism for the morphology evolution of biomimetically prepared hexagonal prism vaterite crystals. The dipolar property of vaterite is proposed to be the driving force for the alignment of nanocrystallites which is the basis for the morphological evolution from single crystal-like spherulite-type

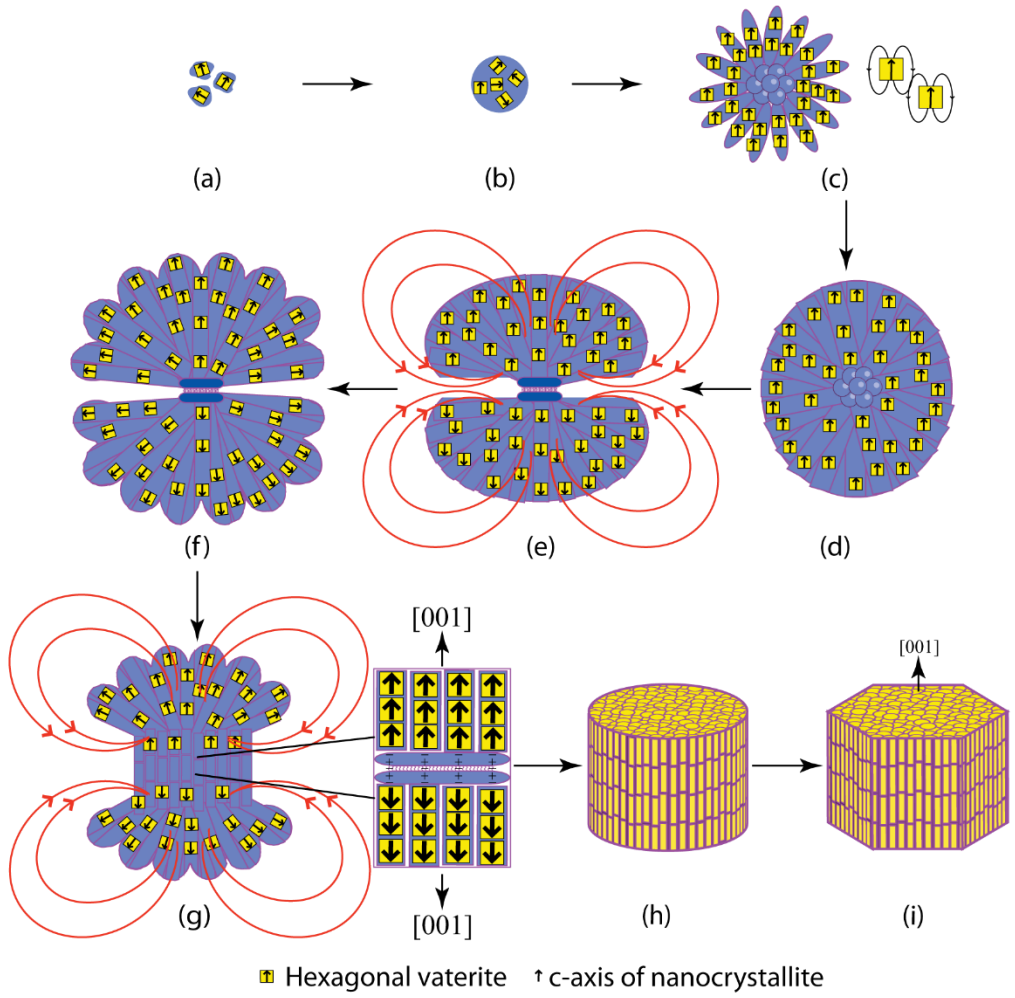

Fig. 7 Schematic drawing representing the formation mechanism and morphology evolution of hexagonal prism vaterite mesocrystals. The arrows represent the *c*-direction of the nanocrystallites which determine the direction of the dipolar fields. Yellow coloured squares symbolise the hexagonal vaterite phase of the nanocrystallites whilst red arc lines in (e) and (g) represent dipolar fields force lines.

particles to hexagonal prism crystals as demonstrated by a proposed mechanism in **Fig. 7**.

At beginning, a crystalline phase of calcium nitrate urea, $Ca(NO_3)_2{\cdot}4[CO(NH_2)_2]$, forms, which is quickly decomposed via the hydrolysis of urea. The synthesis of $CaCO_3$ includes the following two overall reactions:

$$(NH_2)_2CO + 2H_2O \rightarrow 2NH_4^+ + CO_3^{2-}$$

$$Ca^{2+} + CO_3^{2-} \rightarrow CaCO_3$$

$CaCO_3$ nanocrystallites with a diameter of approximately 5 nm are developed. Gelatin molecules coat the surface of the nanoparticles, suppressing any further growth (**Fig. 7a**). These $CaCO_3$/gelatin composite nanoparticles aggregate to form weakly crystalline spherical clusters (**Fig. 7b**), followed by self-attachment into loosely packed needles ordered in a spherulitic manner. To understand the formation of the needles, we assume that all the nanocrystallites may line up with their [001] direction parallel to the longitudinal axis of the needles, governed by the interaction between their dipolar fields. However, we did not observe this type of alignment. Instead, we revealed that all the nanocrystallites in a spherulite particle are parallel to each other (**Fig. 7c**). The vaterite nanocrystallites, embedded in an amorphous precursor/gelatin matrix, change their crystal orientations from randomly orientated in spherical clusters to radially arranged with a needle appearance in spherulite particles, and then to a perfect parallel manner, driven by dipolar fields created in these nanocrystallites. In other words, all the vaterite nanocrystallites can be regarded as nanoscale dipoles. The interaction between these dipoles is strong enough to enable the nanocrystallites to rotate and shift locally within a gelatin soft matrix in the needles until they are perfectly orientated.

The spherulite particles undergo further aggregation of composite into larger ellipsoid shaped particles composed of a much denser array of needles (**Fig. 7d**). The uniform crystal orientation is maintained and the [001] crystal direction is along the long axis of the ellipsoid particles.

Shortly after, an equatorial notch develops on the surface of the ellipsoid particles (**Fig. 7e**). These embryonic-like particles mark the stage, at which the disordered nanocrystallites in the core undergo aggregation and surface crystallisation into a hexagonal vaterite double-plate disc in a similar process to the early stage growth of ZnO twin mesocrystals.[10,41] As the double-plate disc grows in size, lattice tension builds up in the central area of the ellipsoid particles, which instigate the cell-division like splitting. It is believed that the double-plate core detected in the present work has the same property of the ZnO double-plate core, *i.e.* negatively charged gelatin layer in the centre would attract the Ca^{2+} terminal planes in the two plates and leave CO_3^{2-} terminal layers on both the outer surfaces, leading to the formation of a mirror symmetric dipolar field.

Significantly larger twinned cauliflower-like particles (**Fig. 7f**) were then generated. The nanocrystallites about 7 nm in size within the twin cauliflower-like particles are re-arranged further into a radial manner. The change from a smooth surface to a rough surface is believed to be attributed to the re-arrangement of the crystal orientations of the nanocrystallites. The reason for this re-arrangement is that, as the dipolar field of this growing double-plate disc becomes much stronger than the dipolar field of individual nanocrystallites, the orientations of all the nanocrystallites will align along the force lines of this central dipolar field, leading to a 3D radial pattern (**Fig. 7f**).

In a much slower step, intrinsic dipole field force lines originating from the dipole moment of vaterite guide the re-organisation of needles in the twin cauliflower particles into dumbbell structures (**Fig. 7g**). This process begins at the core of the cauliflower-type structure when nanocrystallites located near the double-plate disc undergo a rotation so that their orientation match that of the double-plate disc as shown by the enlarged schematic diagram of the core region in **Fig. 7g**. Consequently, the nanocrystallites in the central 'pedicle' of the twin cauliflower particles line up to form nanorods, which are parallel to each other with their long axes almost parallel to the longitudinal axis of the twin cauliflower particles.

When all the nanocrystallites have re-orientated to form parallel nanorods, both heads of the twin cauliflower particles disappear, leading to a cylindrical morphology (**Fig. 7h**). Surface re-crystallisation then takes place so nanorods with the same orientation can fuse together to create large single crystal-like areas. When these areas expand to cover the whole particle surface, the final morphology of vaterite is a sharp faceted hexagonal prism (**Fig. 7i**). The higher crystallinity at the surface compared to the core region in these prisms has been proven by hydrothermally treating perfect hexagonal prism particles in the 96 h specimen in acidic conditions for 3 h (**Fig. S10, ESI†**). This hollows out the core region of the hexagonal prisms, which is less ordered in comparison with the surface. It can be expected that, in further growth, re-crystallisation will extend from the surface to the core as we often see in reversed crystal growth.[33,34]

Further evidence of dipolar character

According to the proposed mechanism in **Fig. 7,** the dipolar field is believed to be the key driving force for the extraordinary morphology evolution of vaterite. The change of orientations of nanocrystallites observed by SAED and HRTEM presented above strongly indicate the existence of the dipoles in vaterite nanocrystallites and their interactions. However, so far we are unable to detect these dipoles directly through the use of electron holography. More experiments have been arranged to further support this hypothesis.

One way to control the morphology and, in turn reveal the dipolar property of vaterite is to add a salt during the synthesis. This will change the ionic strength of the solution and thus, try to screen the long-range dipolar field by interacting with the polar facets of vaterite. It has previously been demonstrated that the polar faces of ZnO can be addressed separately by anions and cations via specific interactions with the zinc and oxygen terminated facets.[56] In the present work it is expected that the morphology evolution shown in **Fig. 2** would be stopped by the addition of a salt. SEM images of vaterite particles prepared by hydrothermal treatment for 96 h in KCl solution with concentrations of 0.14 M and 0.57 M, respectively are shown in **Fig. S11, ESI†**. At the low KCl concentration, twin cauliflower structures and dumbbell vaterite particles (**Fig. S11a, ESI†**) dominated whereas at the high KCl concentration, the growth never progressed beyond twin cauliflower particles (**Fig. S11b, ESI†**). No hexagonal prism particles were generated using either concentrations of KCl indicating a suppression of the growth along the [001] direction of vaterite. Reduction of growth along the polar planes of vaterite is thought to arise from a strong interaction of the K^+ ions on the O-terminated $(00\bar{1})$ facet and Cl^- ions on the Ca-terminated (001) facet. Previously, when KCl and NaCl was added to ZnO twin mesocrystals the building units were changed from nanorods to nanoplates as the dipolar force was shielded.[41] On the other hand, the formation of the twin cauliflower morphology shown in **Fig. S11a, ESI†** indicates that the influence of KCl to the central double-layer disc particles is limited.

To understand how the addition of KCl as an electrolyte can affect the dipole field of vaterite, it is important to consider Debye length. Debye length is the measure of a charge carrier's net electrostatic effect in solution, and how far those electrostatic effects persist before they are reduced in strength. For a monovalent electrolyte the Debye length, k^{-1} can be expressed as

$$k^{-1} = \sqrt{\frac{\varepsilon_r \varepsilon_0 RT}{2F^2 C_0}}$$

where ε_r is dielectric constant, ε_0 is the permittivity of free space, R is the gas constant, T is the absolute temperature in kelvin, F is the Faraday constant and C_0 is the molar concentration of the electrolyte. Using this equation the Debye screening length for a 0.14 M and a 0.57 M KCl aqueous solution at 100 °C is calculated as 0.75 nm and 0.37 nm, respectively. This implies that with a separation above these values, the two charges can no longer interact by the Coulomb interactions and therefore the external field can be screened out. It is therefore reasonable to expect that the dipolar field driven morphology evolution cannot continue.

Further confirmation of the electric polarity of the vaterite structures and the accuracy of our formation model was accessed by surface staining experiments using charged dye. This staining method has previously successfully illustrated the charges on the surface of dipolar apple-like ZnO[57] and concave-convex calcite mesocrystals[51] and alongside electron microscopic images proved

their formation was driven by a dipole field. The addition of cationic safranin T dye (0.5 g/L) to several vaterite morphologies including ellipsoid, embryonic, twin-cauliflower, dumbbell and hexagonal prisms selectively stained the O-terminated facets red. If the driving force of the morphology evolution is related to dipole field interactions then the terminal surface of the different morphologies would be different as highlighted by the mechanism in **Fig. 7**. For example, the ellipsoid particles would have a positively charged surface at one end and a negatively charged surface at the other, because all the nanocrystallites together with synchronised dipoles in the particles have a uniform orientation. Optical microscopic observations show half the early growth stage ellipsoid particles (**Fig. 8a**) to be stained red (marked by black circles) whilst the remaining surface of the particles was unstained (marked by white circles). This suggests half the surface of the ellipsoid particles is O rich, whilst the other half is Ca rich. The particle marked by the arrow shows a light contrast at the lower half area, implying a profile view direction.

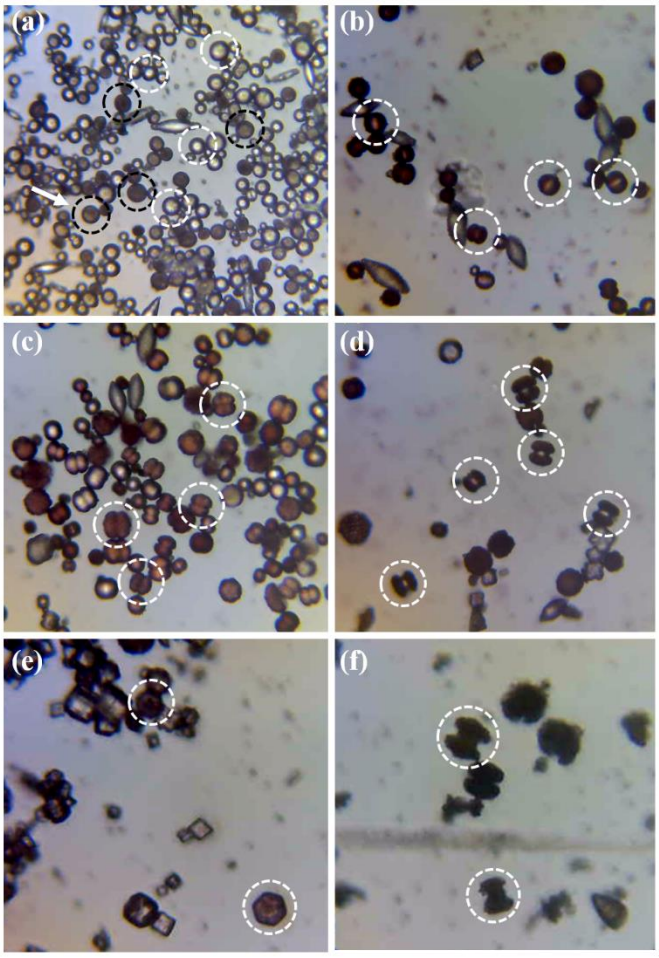

Fig. 8 Optical microscopic images of vaterite mesocrystals stained with cationic safranin T dye. Growth stages include (a) ellipsoid, (b) embryonic, (c) twin-cauliflower, (d) dumbbell, and (e) hexagonal prism particles. (f) Dumbbell particles calcined at 600 °C for 4 h prior to the addition of safranin T dye. The black ring outside all mesocrystals is not dye molecules but fringes formed from the interference between light rays reflected from the surface of the mesocrystal.

Safranin T dye molecules were found to attach to all surfaces of the embryonic (**Fig. 8b**), and twin-cauliflower particles (**Fig. 8c**), showing that their surfaces are all O-terminated. This is consistent with the HRTEM and SAED results where it was proven all nanocrystallites are radially aligned along the *c*-axis. Optical microscopic images of dumbbell (**Fig. 8d**) and hexagonal prism particles (**Fig. 8e**) showed that the cauliflower-type heads of the dumbbells and {001} facets of the hexagonal prisms were stained red whilst the cylindrical 'waist' of the dumbbell and rectangular side faces of the hexagonal prism remained unstained. The structure of the dumbbell heads did not change during the morphology change from twin cauliflower particles, therefore, their surface remained O-terminated. The stained {001} facets of the hexagonal prism particles are also O-terminated due to the guiding of nanocrystallites onto the mirror symmetric double plate disc.

Unstained regions in the dumbbell and hexagonal prism particles are neutral as expected from the uniform orientation of all nanorods. Calcination of dumbbell particles prior to staining with safranin T dye caused dye molecules to attach onto all surfaces of the dumbbell particles (**Fig. 8f**). This suggests that calcination destroyed the ordering of dipolar field by changing the orientation of the nanocrystallites so dye molecules were able to adsorb to all surfaces. All optical microscopic images of stained vaterite mesocrystals are consistent with our experimental observations and the proposed mechanism in **Fig. 7**.

Experimental

Preparation of vaterite specimens: The synthetic method for $CaCO_3$ was the same as that used by Zhan *et al.*[44] in which gelatin (Type B) was used as a structure directing agent. Gelatin is known as a "smart" material because of its sensitivity towards its environment such as temperature and pH. Even a slight deviation can significantly affect its properties.[58] The gelatin, produced from bovine skin, is a single chained series of repeating amino acids obtained from the thermal denaturation of collagen under alkaline conditions.[39] The procedure involved dissolving 1 g gelatin (type B, 225 Bloom, from Sigma) in 10 mL distilled water at 60 °C to form a gel. A mixture of 23.62 g (0.1 mol) $Ca(NO_3)_2{\cdot}4H_2O$ (99%, from Alfa Aesar) and 12.0 g (0.2 mol) urea (ACS grade, from Sigma) was added to the gelatin gel. The final volume is about 35 mL. Therefore, the concentrations of the components are: 28 g/L of gelatin, 2.86 M of $Ca(NO_3)_2{\cdot}4H_2O$, and 5.71 M of urea. The aqueous solution was sealed in a 100 mL PTFE bottle and hydrothermally treated at 100 °C for 96 h. The resulting precipitate was recovered by centrifugation (at G-force 2536 g for 5 min), followed by washing three times with distilled water. The precipitate was then dried at 60 °C overnight. Early stage growth specimens were synthesised under identical conditions except different hydrothermal reaction times of 3 h, 6 h, 23 h and 96 h, were applied. In addition specimens were prepared using different concentrations of gelatin (0 g/L, 7 g/L) and urea (2.86 M) for further investigation of the effects of these chemicals on the crystal growth.

Preparation of charged dye specimens: Safranin T dye was obtained from Sigma-Aldrich and used without further purification. $CaCO_3$ mesocrystals were immersed overnight in a standard dye solution (0.5 g/L) prepared with DI water. The mesocrystals were washed three times with distilled water before placing on a glass slide. After drying the mesocrystals were ready for viewing under the optical microscope.

Preparation of vaterite mesocrystals to study the influence of cations: Gelatin (1 g) was dissolved in 10 mL KCl solution (0.5 M or 2 M) at 60 °C to form a gel. A mixture of $Ca(NO_3)_2{\cdot}4H_2O$ (23.62 g) and

urea (12.0 g) was added to the gelatin gel. The final concentration of KCl is 0.14 M or 0.57 M. The aqueous solution was sealed in a PTFE bottle and hydrothermally treated at 100 °C for 96 h. The resulting precipitate was recovered by centrifugation followed by washing three times with distilled water and drying at 60 °C overnight.

Specimen characterisation: PXRD was performed on a PANalytical Empyrean diffractometer, using Cu Kα radiation (λ = 1.5418 Å). Analysis of the PXRD patterns was carried out using Highscore plus software. SEM images of the specimens were obtained using a JEOL JSM-6700F field-emission gun microscope, operating at 1 to 5 kV with gentle mode. To overcome beam charging problems, the specimen surface was coated with a thin gold film. The FEG-SEM is equipped with an Oxford INCA system for energy dispersive X-ray spectroscopy (EDX), which was applied for examination of the chemical compositions of the specimens. TEM images and SAED patterns were primarily attained using a JEOL JEM-2011 electron microscope operating at an accelerating voltage of 200 kV. This electron microscope is also equipped with an Oxford Link ISIS SemiSTEM EDX system. The TEM and HRTEM images were recorded using a Gatan 794 CCD camera. Additionally, TEM and ADF STEM images were recorded on a Titan Thermis 200 (S)TEM and JEM-ARM200F. A thin slice of a twin cauliflower vaterite mesocrystal was prepared by FIB on dualbeams JEOL JIB-4500, JEOL JIB-4501 and FEI Scios. TGA was carried out on a Stanton Redcroft STA-780 series instrument at a heating rate of 5°C/min under O_2. Light microscopic images were recorded using a BMS D1 series biological microscope.

Conclusions

The present biomimetic vaterite system demonstrates a novel morphology evolution of spherulites to single crystal-like hexagonal prisms. Experimental observations established a very unique case where the nanocrystallites were able to rotate and shift locally within a soft matter matrix. It is remarkable to find vaterite nanocrystallites in the soft matter matrix can be self-aligned into a unidirectional pattern, which transfers to a radial arrangement. Finally the nanocrystallites undergo another re-arrangement into a linear pattern with mirror symmetry along the long axis of the cylindrical particles. Dipole field is proposed to be the driving force of this remarkable morphology evolution. The proposed formation mechanism strongly supports the idea that interactions between the organic and inorganic components can take over and thus direct the morphology. Gelatin not only controls the crystal size at a nanometer scale but may also induce a dipole field in the nanocrystallites. A similar structure to the present work has been observed in pearl oyster, Pinctada fucata[59] where aragonite nanoparticles nucleated with random orientations inside dimples on the surface of the prismatic columns before extending to form nacreous layers where the nanocrystallites were preferentially orientated along the *c*-axis. Further work is needed to obtain direct evidence of dipole field in the samples and to clarify if this dipole field directed re-organisation mechanism can be identified in the formation of many naturally occurring biominerals. Another knowledge gap lies in the following steps, nucleation and the very early growth stages, *i.e.* interactions between a developing mineral and a macromolecular matrix. De Yoreo and colleagues recently tried to address this problem using liquid-cell TEM to visualise the nucleation and growth of $CaCO_3$ in a matrix of polystyrene sulphonate (PSS).[60]

Acknowledgements

The authors would like to thank the Royal Society for the financial support for this international collaboration project (No. JP090443). H.F.G. would like to thank the University of St Andrews for the studentship, Mr Ross Blackley for his help on using the SEM and TEM microscopes and Mrs Sylvia Williamson for doing the TGA experiments in St Andrews, Miss Chia-Ying Chien and Mrs Su-Zhen Ji for help during SEM and FIB experiments at National Taiwan University. We gratefully acknowledge Dr Tomohiro Mihira and Dr Misumi Kadoi from the Ion Beam Application Group and Mr Akira Yasuhara from EM Application Department at JEOL Ltd. for FIB specimen preparation and data collection. Finally, we also thank Dr Emrah Yücelen at FEI Ltd. for FIB specimen preparation and STEM data collection. W.Z. thanks EPSRC for a platform grant (No. EP/K015540/1) and financial support to the Electron Microscopy Laboratory (No. EP/F019580/1).

References

1 L. Addadi and S. Weiner, *Nature*, 1997, **389**, 912.
2 A. Y.-M. Lin, P.-Y. Chen and M. A. Meyers, *Acta. Biomaterialia.*, 2008, **4**, 131.
3 (a) Y. Oaki and H. Imai, *Small*, 2006, ***2***, 66. (b) Y. Oaki, A. Kotachi, T. Miura and H. Imai, *Adv. Funct. Mater*., 2006, **16**, 1633.
4 J. J. Novoa, D. Braga and L. Addadi, *Engineering of Crystalline Materials Properties*; Springer: Dordrecht, The Netherlands, 2008.
5 P. E. Hare and P. H. Abelson, *Carnegie Inst. Wash. Yearb.*, 1965, **64**, 223.
6 A. P. Jackson, J. F. V. Vincent and R. M. Turner, *Proc. R. Soc. Lond.* B, 1988, **234**, 415.
7 A. Lin and A. Meyers, *Mater. Sci. Eng.* A, 2005, **390**, 27.
8 (a) A. Hernández-Hernández, A. B. Rodríguez-Navarro, J. Gómez-Morales, C. Jiménez-Lopez, Y. Nys and J. M. García-Ruiz, *Cryst. Growth Des.*, 2008, **8**, 1495. (b) T. Wang, H. Cölfen and M. Antonietti, *J. Am. Chem. Soc.*, 2005, **127**, 3246. (c) Z. Nan, X. Chen, Q. Yang, X. Wang, Z. Shi and W. Hou, *J. Colloid Interface Sci.*, 2008, **325**, 331.
9 Y.-H. Tseng, H.-Y. Lin, M.-H. Liu, Y.-F. Chen and C.-Y. Mou, *J. Phys. Chem. C*, 2009, **113**, 18053.
10 H. F. Greer, W. Z. Zhou, M.-H. Liu, Y.-H. Tseng and C.-Y. Mou, *CrystEngComm*, 2012, **14**, 1247.
11 J.-Y. Dong, Y.-J. Hsu, D. S.-H. Wong and S.-Y. Lu, *J. Phys. Chem. C*, 2010, **114**, 8867.
12 S. B. Mukkamala and A. K. Powell, *Chem. Commun.*, 2004, 918.
13 A. Finnemore, P. Cunha, T. Shean, S. Vignolini, S. Guldin, M. Oyen and U. Steiner, *Nat. Comm.*, 2012, **3**, 966.
14 (a) T. Matschei, B. Lothenbach and F. G. Glasser, *Cement. Concrete. Res.*, 2007, **37**, 551. (b) J.-F. Chen, H.-M. Ding, J.-X. Wang and L. Shao, *Biomaterials*, 2004, **25**, 723.
15 J. Kawano, N. Shimobayashi, A. Miyake and M. Kitamura, *J. Phys.: Condens. Matter.*, 2009, **21**, 425102.
16 A. Sarkar and S. Mahapatra, *Cryst. Growth Des.*, 2010, **10**, 2129.
17 D. Jin, F. Wang and L. Yue, *Cryst. Res. Technol.*, 2011, **46**, 140.
18 H. F. Greer, W. Z. Zhou and L. Guo, *Miner. Petrol.*, 2015, **109**, 453.

19 (a) Y. S. Han, G. Hadiko, M. Fuji and M. Takahashi, J. Cryst. Growth, 2006, 289, 269. (b) Z. Chen, M. Xin, M. Li, J. Xu, X. Li and X. Chen, *J. Cryst. Growth*, 2014, **404**, 107.
20 R. Demichelis, P. Raiteri, J. D. Gale and R. Dovesi, *Cryst. Growth Des.*, 2013, **13**, 2247.
21 J. Wang and U. Becker, *Am.Mineral.*, 2009, **94**, 380.
22 H. J. Meyer, *Angew. Chem.*, 1959, **71**, 678.
23 S. R. Kamhi, *Acta. Cryst.*, 1963, **16**, 770.
24 L. Kabalah-Amitai, B. Mayzel, Y. Kauffmann, A. N. Fitch, L. Bloch, P. U. P. A. Gilbert and B. Pokroy, *Science*, 2013, **340**, 454.
25 E. Mugnaioli, I. Andrusenko, T. Schüler, N. Loges, R. E. Dinnebier, M. Panthöfer, W. Tremel and U. Kolb, *Angew. Chem. Int. Ed.*, 2012, **51**, 7041.
26 (a) S.-H. Yu, H. Cölfen, A.-W. Xu and W. Dong, *Cryst. Growth Des.*, 2004, **4**, 33. (b) J. Tang and A. P. Alivisatos, *Nano. Lett.*, 2006, **6**, 2701.
27 H. Deng, C. Liu, S. Yang, S. Xiao, Z.-K. Zhou and Q.-Q. Wang, *Cryst. Growth Des.,* 2008, **8**, 4432.
28 M. Shang, W. Wang, J. Ren, S. Sun and L. Zhang, *CrystEngComm*, 2010, **12**, 1754.
29 D. P. Grigor'ev, *Ontogeny of Minerals*; Israel Program for Scientific Translations: Jerusalem, 1965.
30 R. Beck, E. Flaten and J.-P. Andreassen, *Chem. Eng. Technol.*, 2011, **34**, 631.
31 Y. O. Punin, *Zap. Vses. Mineral. Ova*., 1981, **110**, 666 (Russian).
32 X.-H. Guo, S.-H. Yu and G.-B. Cai, *Angew. Chem. Int. Ed*., 2006, **45**, 3977.
33 (a) H. F. Greer, P. S. Wheatley, S. E. Ashbrook, R. E.Morris and, W. Z. Zhou, *J. Am. Chem. Soc.*, 2009, **131**, 17986. (b) W. Z. Zhou, *Adv. Mater*. 2010, **22**, 3086. (c) A. W. Ritchie, M. I. T. Watson, R. Turnbull, Z. Z. Lu, M. Telfer, J. E. Gano, K. Self, H. F. Greer and W. Z. Zhou, *CrystEngComm*, 2013, **15**, 10266.
34 X. Y. Chen, M. H. Qiao, S. H. Xie, K. N. Fan, W. Z. Zhou and H. Y. He, *J. Am. Chem. Soc.*, 2007, **129**, 13305.
35 (a) H. D. Keith and F. J. Padden, *J. Appl. Phys.*, 1963, **34**, 2409. (b) J. H. Magill, *J. Mater. Sci.*, 2001, **36**, 3143.
36 X. Zhang, Z. Zhang and S. C. Glotzer, *J. Phys. Chem. C*, 2007, **111**, 4132.
37 H. Tlatlik, P. Simon, A. Kawska, D. Zahn and R. Kniep, *Angew. Chem. Int. Ed*., 2006, **45**, 1905.
38 (a) X. F. Yang, J. X. Fu, C. J. Jin, J. Chen, C. L. Liang, M. M. Wu and W. Z. Zhou, *J. Am. Chem. Soc*., 2010, **132**, 14279. (b) H. Q. Zhan, X. F. Yang, C. M. Wang, J. Chen, Y. P. Wen, C. L. Liang, H. F. Greer, M. M. Wu and W. Z. Zhou, *Cryst. Growth Des.*, 2012, **12**, 1247.
39 L. P. Bauermann, A. Del Campo, J. Bill and F. Aldinger, *Chem. Mater*., 2006, **18**, 2016.
40 Y. Yao, W. Dong, S. Zhu, X. Yu and D. Yan, *Langmuir*, 2009, **25**, 13238.
41 M.-H. Liu, Y.-H. Tseng, H. F. Greer, W. Z. Zhou and C.-Y. Mou, *Chem. Eur. J.*, 2012, **18**, 16104.
42 H. Imai, N. Tochimoto, Y. Nishino, Y. Takezawa and Y. Oaki, *Cryst. Growth Des*., 2012, **12**, 876.
43 K. Matsumoto, N. Saito, T. Mitate, J. Hojo, M. Inada and H. Haneda, *Cryst. Growth Des.*, 2009, **9**, 5014.
44 J. Zhan, H.-P. Lin and C.-Y. Mou, *Adv. Mater.*, 2003, **15**, 621.
45 M. Jitianu and D. V. Goia, *J. Colloid Interface Sci.*, 2007, **309**, 78.
46 L. Qiao and Q. L. Feng, *J. Cryst. Growth*, 2007, **304**, 253.
47 K. Yasui and K. Kato, *J. Phys. Chem. C*, 2012, **116**, 319.
48 (a) S. Busch, H. Dolhaine, A. DuChesne, S. Heinz, O. Hochrein, F. Laeri, O. Podebrad, U. Vietze, T. Weiland and R. Kniep, *Eur. J. Inorg. Chem.*, 1999, **1999**, 1643. (b) P. Simon, D. Zahn, H. Lichte and R. Kniep, *Angew. Chem. Int. Ed.*, 2006, **45**, 1911.
49 R. Kniep and P. Simon, *Angew. Chem. Int. Ed.*, 2008, **47**, 1405.
50 P. Simon, U. Schwarz and R. Kniep, *J. Mater. Chem.*, 2005, **15**, 4992.
51 T. Wang, M. Antonietti and H. Cölfen, *Chem. Eur. J.*, 2006, **12**, 5722.
52 G.-T. Zhou, Q.-Z. Yao, J. Ni and G. Jin, *Am. Mineral.*, 2009, **94**, 293.
53 Y. Xu, G. Ma and M. Wang, *Cryst. Growth Des.*, 2014, **14**, 6166.
54 P. Simon, E. Rosseeva, J. Buder, W. Carrillo-Cabrere and R. Kniep, *Adv. Funct. Mater.*, 2009, **19**, 3596.
55 A. Kawska, O. Hochrein, J. Brickmann, R. Kniep and D. Zahn, *Angew. Chem. Int. Ed*., 2008, **47**, 4982.
56 C. Lizandara-Pueyo, M. C. Morant-Miñana, M. Wessig, M. Krumm, S. Mecking and S. Polarz, *RSC Adv.*, 2012, **2**, 5298.
57 Z. Liu, X. D. Wen, X. L. Wu, Y. J. Gao, H. T. Chen, J. Zhu and P. K. Chu, *J. Am. Chem. Soc.*, 2009, **131**, 9405.
58 J. Mao, S. Kondu, H.-F. Ji. and M. J. McShane, *Biotechnol Bioeng*, 2006, **95**, 333.
59 K. Saruwatari, T. Matsui, H. Mukai, H. Nagasawa and T. Kogure, *Biomater.*, 2009, **30**, 3028.
60 P. J. M. Smeets, K. R. Cho, R. G. E. Kempen, N. A. J. M. Sommerdijk and J. J. de Yoreo, *Nat. Mater.*, 2015, **14**, 394.

